

Research Article

Effect of Longitudinal-External-Fins on Fluid Flow Characteristics for Wing-Shaped Tubes Bundle in Crossflow

Sayed Ahmed E. Sayed Ahmed, Osama M. Mesalhy, and Mohamed A. Abdelatif

Mechanical Power Engineering Department, Faculty of Engineering, Zagazig University, Zagazig 44519, Egypt

Correspondence should be addressed to Mohamed A. Abdelatif; eng_aboatia@yahoo.com

Received 4 July 2015; Revised 15 September 2015; Accepted 16 September 2015

Academic Editor: Shou-Shing Hsieh

Copyright © 2015 Sayed Ahmed E. Sayed Ahmed et al. This is an open access article distributed under the Creative Commons Attribution License, which permits unrestricted use, distribution, and reproduction in any medium, provided the original work is properly cited.

A numerical study is conducted to clarify fluid-flow characteristics, pressure drop coefficient (P_{dc}), and the average skin friction coefficient ($C_{f,m}$) for wing-shaped-tubes bundle with longitudinal fins at downstream side of the tube using the commercial CFD FLUENT software package. The air-side Re_a ranges from 1800 to 9700. The tubes are employed with various fin heights (h_f) and fin thicknesses (δ) such as $2 \text{ mm} \leq h_f \leq 12 \text{ mm}$ and $1.5 \text{ mm} \leq \delta \leq 3.5 \text{ mm}$ at the considered Re_a range. Results indicate that ΔP_a increases with Re_a for all h_f . P_{dc} decreases with Re_a for all h_f values for $1800 \leq Re_a \leq 4200$ and then increases for $4200 \leq Re_a \leq 10000$. Lowest values of ΔP_a , P_{dc} , and pumping power (PP) occurred at $h_f = 6 \text{ mm}$. Values of P_{dc} for $h_f = 6 \text{ mm}$ are lower than those of NOF and $h_f = 2 \text{ mm}$ by about 73 % and 32 %, respectively, at $Re_a = 4000$. $C_{f,m}$ decreases with Re_a . δ has negligible effect on $C_{f,m}$. ΔP_a increases for $1.5 \text{ mm} \leq \delta \leq 2.5 \text{ mm}$ while ΔP_a decreases with $2.5 \text{ mm} < \delta \leq 3.5 \text{ mm}$ for the considered Re_a range except for $Re_a = 1850$.

1. Introduction

Finned tube heat exchangers are extensively employed in chemical engineering, refrigeration, and HVAC applications. The dominant thermal resistance is usually on the air side in practical applications, and therefore the use of finned surfaces on the air side is very common to effectively improve the overall thermal performance of heat exchangers. Depending on the application, various fin patterns such as plate, louver, convex louver, and wavy fin are used.

There is, of course, an associated increase in ΔP_a due to the increase of friction and the drag contribution from the finite thickness of the interrupted fins. The typical tube geometries used in most of heat exchangers are circular and elliptical ones. A detailed survey on tube heat exchangers with different types of fin configurations is presented as follows.

Chen et al. [1] applied the inverse scheme of the finite difference method in conjunction with the least-squares scheme and experimental temperature data to estimate the air flow and heat transfer characteristics on vertical plate finned tubes heat exchanger in forced convection for various air speed (V_a) and fin spacing (S). Results showed that the fin

efficiency (η_f) values decreased with increasing S and V_a values. A combined numerical and experimental study of plate finned tubes heat exchangers was examined by Jang et al. [2]. They presented detailed numerical results of ΔP_a and h_a , but experimental results were not enough. A systematic study on heat and friction characteristics of plate finned tubes heat exchangers was experimentally investigated by Wang et al. [3]. Results are limited to the cases with relatively large fin pitch heat exchangers.

Khudheyer and Mahmoud [4] carried out a numerical study on finned tubes heat exchanger to make CFD simulations and validated the results against experimental data. Ten different inlet Re_a 's ranging from 330 to 7000 were simulated for turbulence models of laminar, k -epsilon, and SST k -omega. Reasonable agreement was found between the simulated and experimental data.

Three-dimensional CFD simulations were carried out to investigate heat transfer and fluid flow characteristics of three-row plain finned tubes heat exchangers using FLUENT software by Ghori and Kirar [5]. Pressure drop characteristics of the heat exchanger were investigated for Re ranging from 330 to 7000. Fluid flow was simulated and results compared

for laminar flow model, turbulent flow models k - ϵ , and SST k - ω , with steady-state solvers to determine pressure drop ΔP , and temperature fields. Model validation was carried out by comparing simulated values of friction factor (f) with experimental results by Wang et al. [3]. Reasonable agreement between simulated and experimental data was found, thus proving that the FLUENT software is sufficient for simulating the flow fields in finned tubes heat exchangers.

Yan and Sheen [6] have carried out an experiment to investigate the heat transfer and pressure drop characteristics of finned tubes heat exchangers with plate, wavy, and louvered finned tubes. They found that, at the same Re_a , louvered finned heat exchanger shows larger values of f compared with those for plate finned tubes one. Wolf et al. [7] studied the air flow and heat transfer performance of a wavy finned tubes heat exchanger by numerical and experimental methods. The air side pressure drop characteristics were successfully modeled using the CFD software FLUENT. The numerical results were validated with the experimental ones and the deviation was within 8%. Tang et al. [8] carried out an experimental and numerical study on the air side performance of finned tubes heat exchangers with various fin configurations, such as crimped spiral, plain, and slit finned tube heat exchanger. It was found that the heat exchanger with the crimped spiral fin has better performance than those for the other configurations. Also, it is found that heat exchanger with slit fins offers the best performance at higher Re_a .

Leu et al. [9] conducted a numerical simulation for louvered fin and tube heat exchangers having circular and oval tube configurations. The effects of the geometrical parameters such as louver angle (θ), louver pitches (L_p), and louver length (L_l) were discussed. Toen et al. [10] worked on the interaction between the flow behavior (flow deflection and transition to unsteady flow) and the thermohydraulic performance of heat exchanger with an inclined louvered fin design. In this experiment, the impacts of fin pitch (F_p), (θ), and Re_a were discussed in detail. Li and Wang [11] conducted an experimental study on the air side heat transfer and pressure drop characteristics of brazed aluminum heat exchangers, with multiregion louver fins and flat tubes. They found that ΔP_a tends to decrease with increasing Re_a and increase with the number of louvers.

Heat transfer and pressure drop characteristics for longitudinally finned tubes banks had been carried out by Sparrow and Kang [12]. The investigated geometrical parameters included the placement of the fins at the tube frontal side, at the rear, and at both. Results indicated that finned tube actually reduced the pressure drop relative to the corresponding unfinned tube. For the same pressure drop, finning yields significantly greater enhancements. At fixed mass flow, greater enhancements were attained with increased-diameter unfinned tubes, but at a high penalty in pressure drop and pumping power.

An experimental investigation had been conducted by Ibrahim and Moawed [13] to clarify heat transfer characteristics and entropy generation for individual elliptical tubes with LF. The investigated geometrical parameters included the placement of the fins at the front of the tube, at the rear of the tube, and at both. The air Re_a ranged from about

4.7×10^3 to 3.96×10^4 . The analysis of the entropy generation is based on the principle of minimizing the rate of total entropy generation that includes the generation of entropy due to heat transfer and friction losses. Results indicated that the fin position on the elliptical tube has an effect on the results of f and irreversibility ratio (Φ). The correlations of average f and Φ with Re_a were presented.

Torabi and Zhang [14] studied, analytically, the temperature distribution within convective-radiative straight fins with simultaneous variation of k , h_a , surface emissivity (B), and internal heat generation with temperature. They assumed nonzero convective and radiative sink temperatures for their analysis. Rectangular, triangular, convex, and exponential LF were considered. Calculations are carried out using the well-known, approximate analytical differential transformation method (DTM). From illustrative data, in this paper, one could find that fin with the rectangular profile has the highest η_f comparing to the other three profiles. So, this paper showed the validity and great potential of the DTM for nonlinear problems in science and engineering applications.

There are few reports of implementation of longitudinal finned tubes heat exchanger (LFTH) for wing-shaped tubes. Notably, there are no reports on LFTH enhancement for multirow wing-shaped tubes heat exchangers. Therefore, the aim of the present study is to numerically investigate, by the aid of commercial code FLUENT version 6.3.26, the air flow, skin friction characteristics, and pressure contours through a wing-shaped tubes bundle in staggered arrangement with the placement of various longitudinal fins with different h_f and δ at the downstream side of the tube. h_f and δ are $2 \text{ mm} \leq h_f \leq 12 \text{ mm}$ and $1.5 \text{ mm} \leq \delta \leq 3.5 \text{ mm}$ for the considered Re_a range.

2. Description of the Computational Model

The numerical model is used to study the hydrodynamic and thermal performance of a staggered wing-shaped tubes bundle with LF mounted at the rear side of the tubes. The computational model considered, in the present work, is a simple design of air to water heat exchanger. The heat exchanger domain consists of three connected rectangular duct sections, entrance, tube bundle, and exit, as shown in Figure 1. The entrance section dimensions are 305 mm, 305 mm, and 320 mm as height, width, and length, respectively. The exit section is similar to the entrance one. The tube bundle section is fixed between the two above-mentioned sections.

Schematic plane of the numerical domain for the cross-flow over the tube bundle, shown in Figure 2, consists of 22 wing-shaped tubes, which are distributed through three successive rows in addition to four half dummy ones. The cross-sectional dimensions of wing-shaped tube, drawn from 1 mm thick, 22.5 mm outer diameter circular copper tube with 305 mm length, are shown in Figure 3. LF of copper sheet having a width of 305 mm and varied h_f and δ such as $2 \text{ mm} \leq h_f \leq 12 \text{ mm}$ and $1.5 \text{ mm} \leq \delta \leq 3.5 \text{ mm}$ are welded on the downstream side of the tube surface. Longitudinal S_L and transverse S_T tube pitches of 37 mm were kept constant. Hot air is forced to flow over the external cooled surface of the

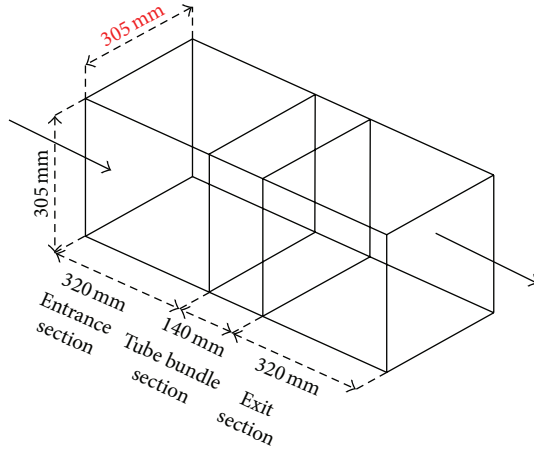


FIGURE 1: Heat exchanger domain.

tubes with different Re_a . Flowing air velocity (V_{ai}) is varied from 1.33 to 7 m/s, yielding Re_a ranging from 1.8×10^3 to 9.7×10^3 . Tubes surface temperature is kept constant.

3. Numerical Investigation

3.1. Problem Description and Boundary Conditions. Since the tube length is much greater than its equivalent diameter, the flow across the tube bundle is considered two-dimensional flow one. The geometry of the numerical model including the boundary conditions is shown in Figure 2. The numerical solution is carried out by solving the governing equations of mass, momentum, and energy under the following assumptions; the flow is incompressible, steady, and turbulent. The fluid properties are constant; also, the effects of buoyancy forces and radiation are neglected. Based on these assumptions the governing equations can be set as

$$\begin{aligned} \frac{\partial}{\partial x_i} (\rho V_i) &= 0, \\ \frac{\partial}{\partial x_j} (\rho V_i V_j) &= -\frac{\partial p}{\partial x_i} + \frac{\partial \tau_{ij}}{\partial x_j}, \\ \frac{\partial}{\partial x_i} [V_i (\rho E + p)] &= \frac{\partial}{\partial x_i} \left(k \frac{\partial T}{\partial x_i} \right), \end{aligned} \quad (1)$$

where i is a tensor indicating 1 and 2, τ_{ij} is the viscous stress tensor, and k is the fluid effective thermal conductivity.

Commercial CFD software FLUENT 6.3.26 is used to solve the governing equations. RNG $k-\varepsilon$ turbulence model is used to simulate the flow fluctuations because it is reported to be more responsive to the effects of flow strain rate, which significantly improves the accuracy for rapidly strained flows, such as the case in reactive swirling flows. Also the RNG $k-\varepsilon$ model shows better performance than the standard $k-\varepsilon$ model in the prediction of heat transfer as examined by Hu and Sun [15]. The RNG $k-\varepsilon$ model has shown an excellent agreement between numerical and experimental results for an isothermal flow over backward facing step (Yakhot et al.)

[16]. The near wall region is treated using the enhanced wall method, which is capable of predicting the flow separation and recirculation behind bluff bodies, FLUENT [17].

3.2. Mesh Generation and Discretization. The geometry and mesh of the computational model described in the previous section are generated separately using GAMBIT 2.4.6. Quad/Map, Tri/Pave, and boundary layer meshing scheme is used in the present study with refining the mesh near walls and beside sharp edges.

Figure 4 shows the configuration of the computational mesh. Over the computational grid, the conservation equations as well as the turbulence equations are discretized using the second-order upwind scheme. The velocity pressure coupling is solved using SIMPLE algorithm. The solution is considered converged when the scaled residual of the energy equation reaches 10^{-7} and the scaled residuals of other equations reach 10^{-4} .

To test the dependence of the numerical results on the grid density, calculations are undertaken with different mesh densities in the x and y directions as recommended by FLUENT [17]. The first grid points adjacent to the walls were kept at y^+ values between 1 and 5. The grid sensitivity analysis is carried out, mainly, to obtain grid independent temperature distributions. The computational results of h_a for the tube bundle are varied to give about 2.1% deviation when the number of grids ranges from 250,000 to 420,000. On the other hand, when the grid size ranges from 300,000 to 420,000, only 0.12% variation in h_a is obtained as shown in Figure 5. It is clear that the effect of grid size on the computed results diminishes for grids of 300,000 nodes. Therefore, the computing time can be, drastically, cut down to save computing time without a penalty of poor accuracy.

4. Data Reduction

4.1. Fluid Flow Considerations. The pressure drop coefficient, P_{dc} , as defined below in (2) represents the ratio of the total pressure drop of the moving air through the tube bundle ΔP_a to its dynamic pressure:

$$P_{dc} = \frac{2\Delta P_a}{\rho_{af} \cdot V_{ai}^2}, \quad (2)$$

where ΔP_a is the pressure drop through the tube bundle and ρ_{af} is the air film density and V_{ai} is the inlet air velocity.

Re_a and skin friction coefficient C_f are denoted as

$$Re_a = \frac{\rho_{af} V_{ai} D_{eq}}{\mu_{af}}, \quad (3)$$

$$C_f = \frac{\tau_w}{0.5\rho V_a^2},$$

where τ_w is the wall shear stress (N/m^2).

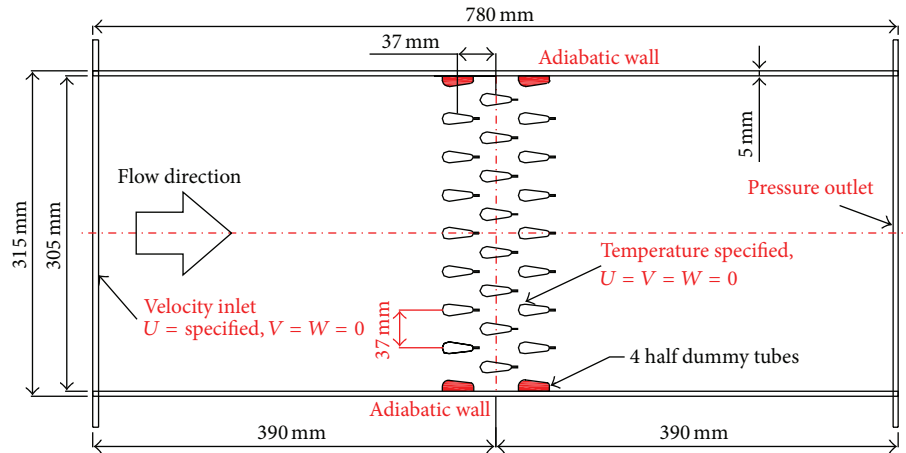


FIGURE 2: Schematic plane of the numerical domain with boundary conditions.

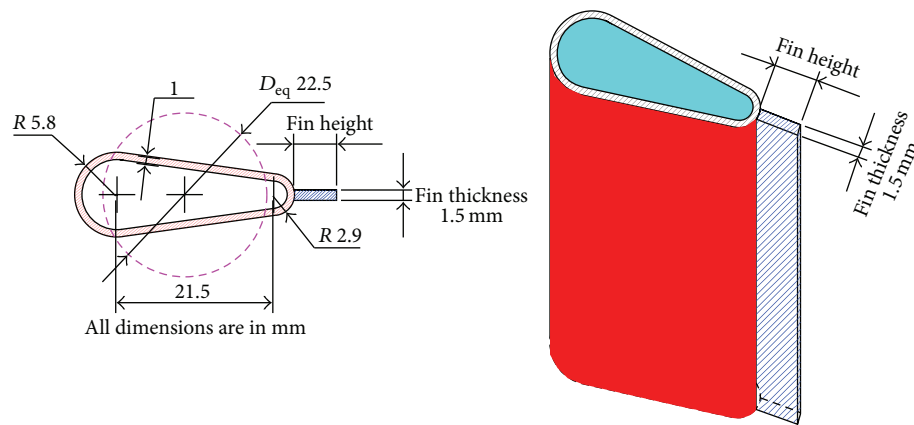


FIGURE 3: Wing-shaped tube cross-sectional dimensions with longitudinal fin.

5. Results

5.1. Validation of the Computational Model. The numerical results of the present study are validated with the corresponding experimental ones obtained by Sayed Ahmed et al. [18]. Figure 6 shows the validation of the experimental and numerical values of P_{dc} versus Re_a for wing-shaped tubes without fins (NOF). The average estimated error between the numerical and experimental results, at considered Re_a , does not exceed 9%.

5.2. Effect of h_f and Re_a at Constant ($\delta = 1.5$ mm) on Fluid Flow Characteristics of Heat Exchanger Performance. From the earliest study, it has been found that the wing-shaped tubes heat exchangers have higher performance than those with circular and elliptical ones (Sayed Ahmed et al.) [18, 19]. Further performance improvement requires the elimination of heat transfer deficiency in certain regions over the wing-shaped tubes. This suggests the placement of extended surface and/or protrusions in the deficient regions, where the separation of flow makes the heat transfer, mainly, by convection.

Fins is conducting heat outside of this region to the main flow where forced convection is dominant. Thus, fins act as a heat transfer cascade where the heat transfer conduction through the fins is followed by convection to the main flow downstream.

5.2.1. Air Flow Characteristics. Changing h_f for the wing-shaped tubes could affect the location at which separations and wakes were formed as well as the turbulence generation rate in the flow passing over the tubes. This in turn would have a direct effect on the resultant ΔP and on the heat exchange during the air cooling process. So, results will be portrayed by presenting the flow streamlines, velocity, and turbulent kinetic energy contours.

Flow-path-lines and velocity contours across the wing-shaped tubes of the studied bundle arranged for different fin heights are illustrated in Figures 7–10. Up to 12 mm fin height as shown in Figure 7, at $Re_a = 1.8 \times 10^3$, for the arrangement of different fin heights there are three flow separation zones, two on the lateral sides and one at the rear surfaces of the tubes. This region is considered as a dead zone, where the separation of the flow makes the heat transfer mainly by

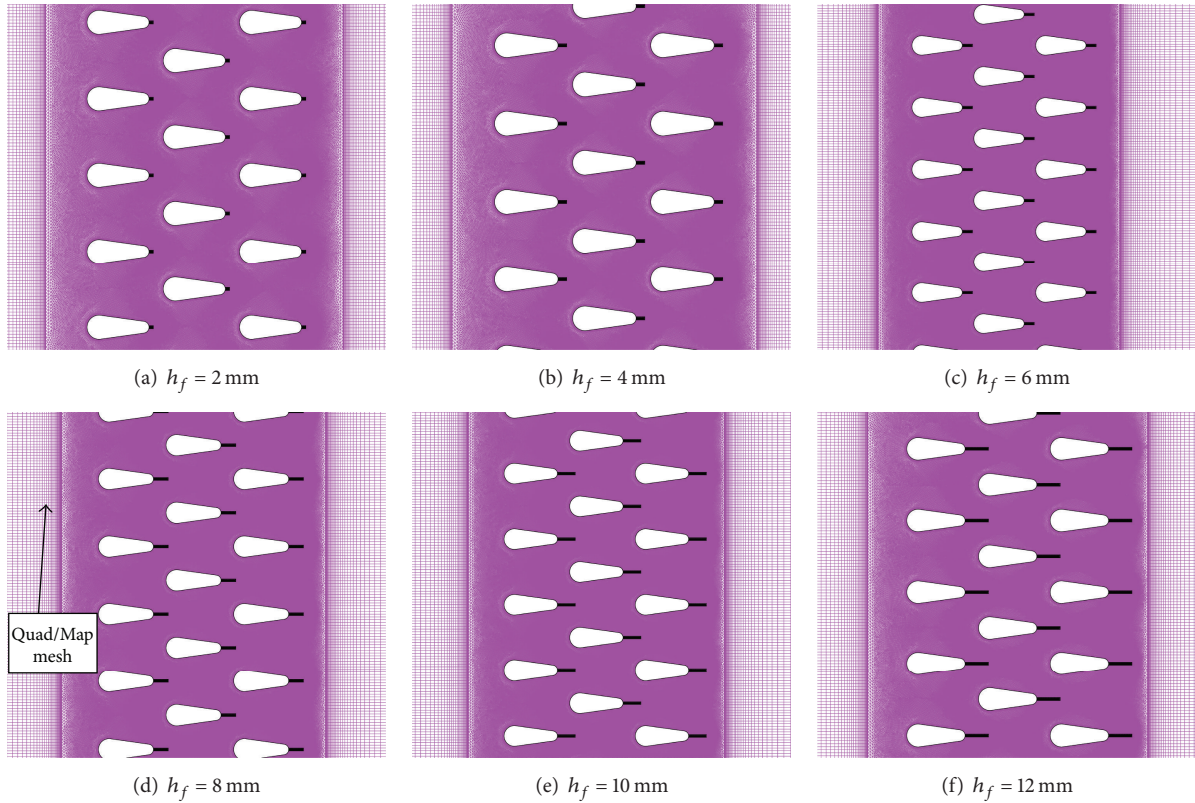


FIGURE 4: Mesh configurations for the domain of the tubes bundle.

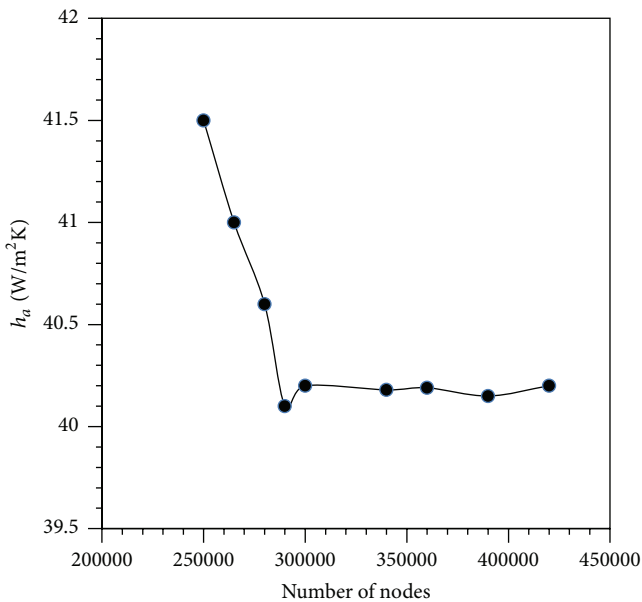


FIGURE 5: Effect of number of nodes of grid points on the computational h_a .

natural convection. Flow separations occurred, as a result of travelling of the boundary layer far enough against an adverse pressure gradient that makes the velocity of the boundary layer fall, almost, to zero. On the other hand, flow separation

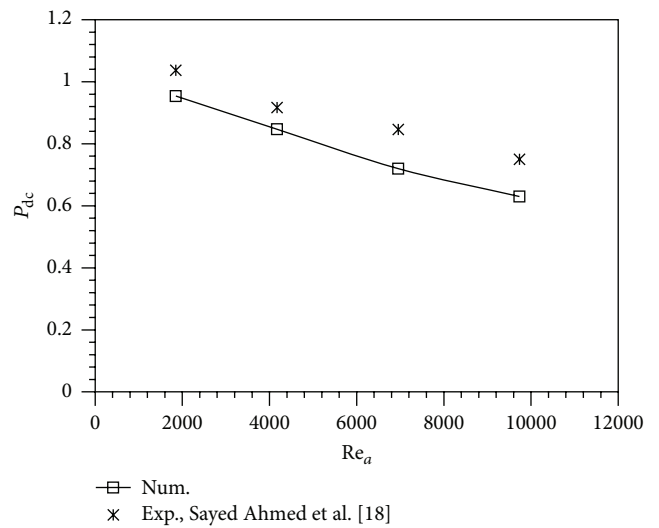


FIGURE 6: Validation of the experimental and numerical values of P_{dc} versus Re_a for NOF.

can occur as a result of the increase of the pressure drag caused by the pressure differential of the flowing air between the frontal and rear surfaces of the tube.

On the other hand, for high Re_a , as shown in Figure 8, separations and secondary flows intensity occurred, mainly, on the rear surfaces of the tubes. It is seen from Figure 8 that,

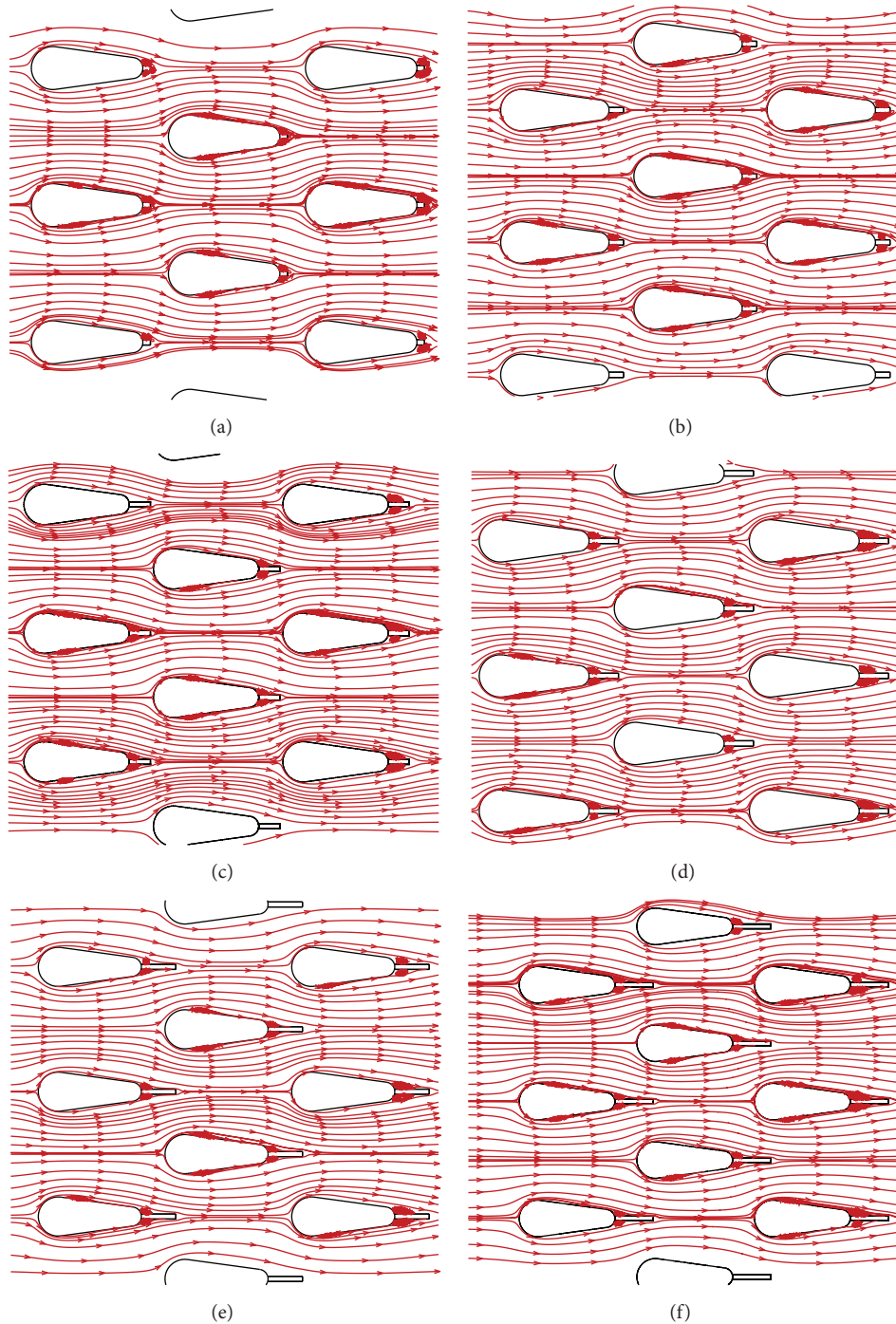


FIGURE 7: Air flow path-lines of the wing-shaped tubes bundle for different fin heights (h_f) at $Re = 1800$: (a) $h_f = 2$ mm, (b) $h_f = 4$ mm, (c) $h_f = 6$ mm, (d) $h_f = 8$ mm, (e) $h_f = 10$ mm, and (f) $h_f = 12$ mm.

with increasing fin height, eddies and vortices at lateral tube surfaces disappeared. This is due to the fact that, for high Re_a , the flow becomes more energetic enabling the boundary layer to travel further along with the tube surface before separation occurs resulting, only, in a narrower wake at the rear surface of the tube.

As seen from Figures 9 and 10, the air flow is strongly accelerated in the passages between tubes. With increasing

of fin heights and/or Re_a the flow is strongly guided between the tubes and the deficient flow separation zones are delayed and/or disappeared. Also, the levels of turbulence and formation of vortices through the passages of the bundle are increased.

Figures 11 and 12 present the turbulent kinetic energy contours through the wing-shaped tubes of the bundle for both low and high Re_a , which is defined as the mean kinetic

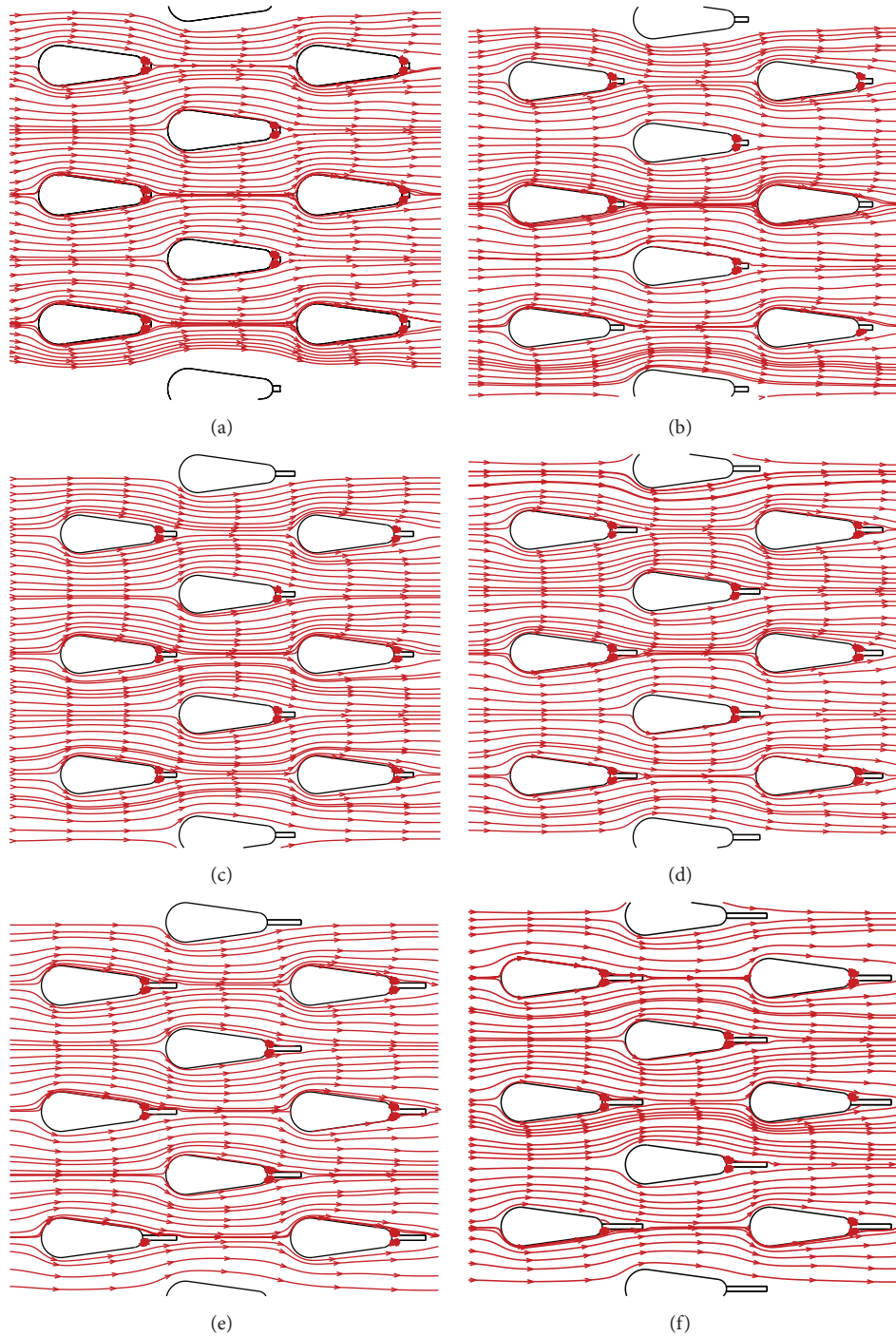


FIGURE 8: Air flow path-lines of the wing-shaped tubes bundle for different fin heights (h_f) at $Re = 9700$: (a) $h_f = 2$ mm, (b) $h_f = 4$ mm, (c) $h_f = 6$ mm, (d) $h_f = 8$ mm, (e) $h_f = 10$ mm, and (f) $h_f = 12$ mm.

energy per unit mass associated with eddies in turbulent flow. Physically, the turbulent kinetic energy produced by friction and buoyancy forces or through external forcing at low-frequency Eddy scales (integral scale) is characterized via root-mean-square method (RMS). Turbulence kinetic energy is transferred down the turbulence energy cascade and dissipated by viscous forces at the Kolmogorov scale (smallest

scales in the spectrum that form the viscous sublayer range). It is found that the turbulent kinetic energy is larger in magnitude in the case of higher Re_a . This, in turn, enhances the fluid flow characteristics. It is, also, seen from the figures that there is a direct proportionality between Re_a and the values of turbulent kinetic energy (k) but the numerical results show that the values of k at the exit section of

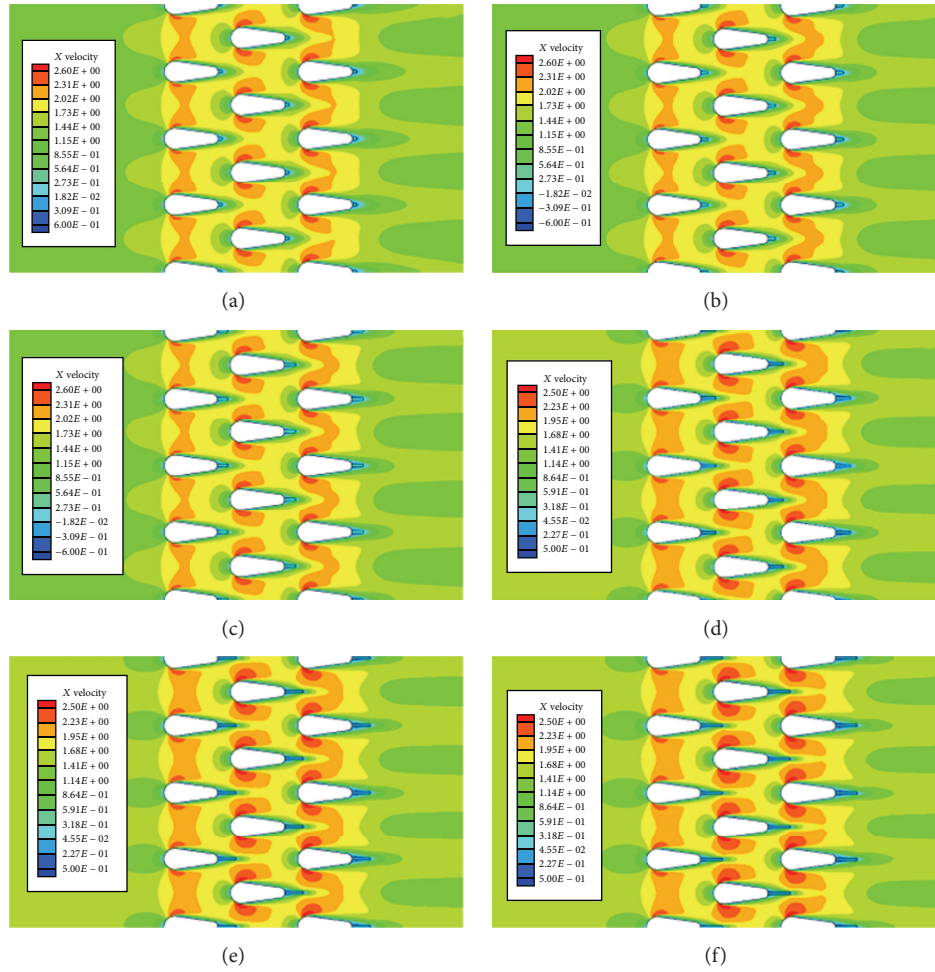


FIGURE 9: Velocity contours (m/s) of the wing-shaped tubes bundle for different fin heights (h_f) at $Re = 1800$: (a) $h_f = 2$ mm, (b) $h_f = 4$ mm, (c) $h_f = 6$ mm, (d) $h_f = 8$ mm, (e) $h_f = 10$ mm, and (f) $h_f = 12$ mm.

the bundle are always greater than those at the inlet one for considered Re_a range, so the bundle works as a turbulence generator which leads to an increase in the heat transfer between tubes and flowing air. With the increasing of h_f the values of k increase at the fin tip leading to the enhancement of heat transfer over the following rows of the bundle. So, the fin acts as a turbulent generator.

5.2.2. Air Flow Pressure Drop through the Bundle. Figures 13 and 14 demonstrate the static pressure contours through the bundle. It can be seen that the pressure has the highest values at the stagnation point on the frontal portion of each tube, at which the flow velocity tends to be zero. As the flow passes over the tube surface, the pressure decreases until reaching its lowest value at the tube lateral surface.

Figure 15 shows the variation of ΔP_a versus Re_a at different h_f . It is seen from the figure that ΔP_a increases with the increase of Re_a for different h_f . Figure 16 shows the variation of ΔP_a versus various h_f at different values of Re_a . ΔP_a decreases with h_f for $2 \text{ mm} \leq h_f \leq 6 \text{ mm}$, while there is no significant change of ΔP_a for $6 \text{ mm} < h_f \leq 12 \text{ mm}$

except for slight increasing of ΔP_a at $6 \text{ mm} < h_f \leq 12 \text{ mm}$ for $Re_a = 9700$. Lowest values of ΔP_a occurred for arrangements of $h_f = 6 \text{ mm}$.

Figure 17 shows the variation of P_{dc} versus Re_a at different h_f . It is seen from the figure that P_{dc} decreases with Re_a for NOF. P_{dc} has the highest values for all studied h_f at $Re_a = 2000$ and decreases with the increase of Re_a in the range of $1800 \leq Re_a \leq 4200$ and then increases for $4200 \leq Re_a \leq 10000$ for all tested fins. Lowest values of P_{dc} occurred at $h_f = 6 \text{ mm}$. The values of P_{dc} for $h_f = 6 \text{ mm}$ are lower than those of NOF and $h_f = 2 \text{ mm}$ by about 73% and 32%, respectively, at $Re_a = 4000$.

Figure 18 shows the variation of P_{dc} versus various h_f at different values of Re_a . P_{dc} decreases with h_f for $2 \text{ mm} \leq h_f \leq 6 \text{ mm}$, while P_{dc} increases with $6 \text{ mm} < h_f \leq 12 \text{ mm}$ for the considered Re_a range.

These results can be attributed to the fact that the overall drag consists of two combined parts; one presents the pressure drag while the other presents the friction drag. The friction drag is more dominant than the pressure drag at the lower Re_a , thus leading to higher pressure drop while the opposite is true at higher Re_a . In the case of high Re_a ,

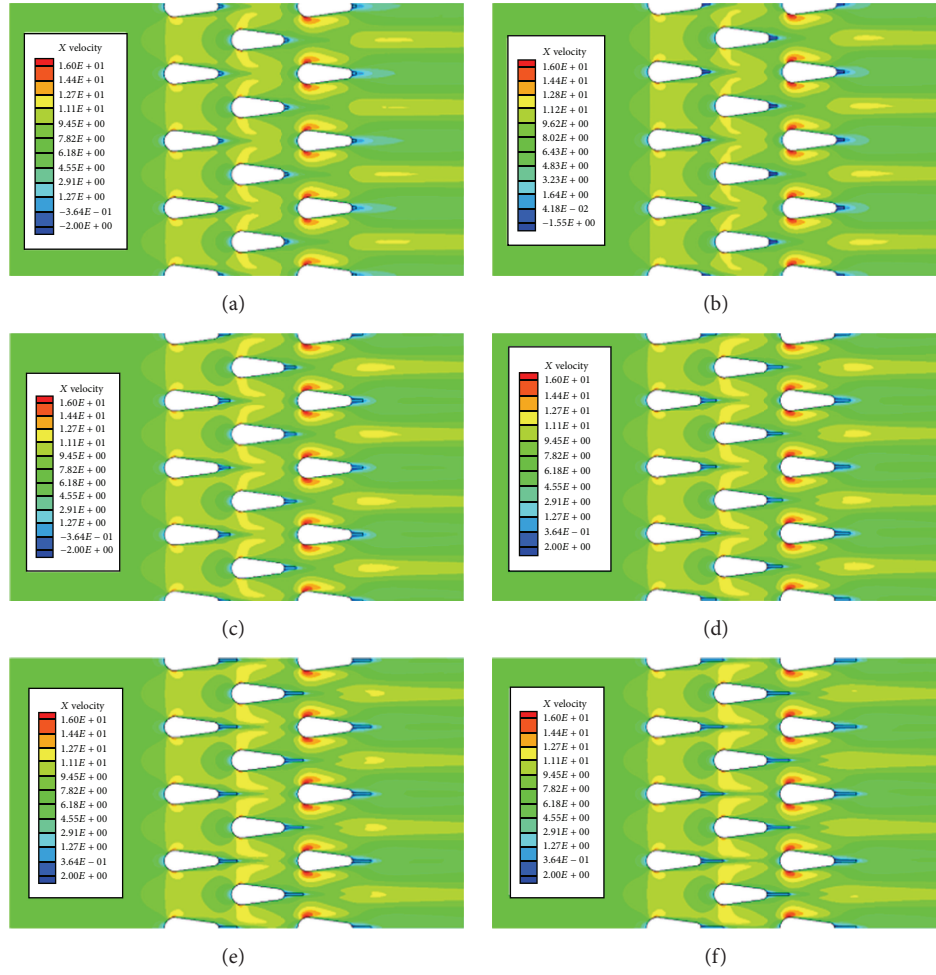


FIGURE 10: Velocity contours (m/s) of the wing-shaped tubes bundle for different fin heights (h_f) at $Re = 9700$: (a) $h_f = 2$ mm, (b) $h_f = 4$ mm, (c) $h_f = 6$ mm, (d) $h_f = 8$ mm, (e) $h_f = 10$ mm, and (f) $h_f = 12$ mm.

the effect of viscosity is less dominant and the total drag is rather affected by the inertia forces. As the flow tends to shift towards more turbulent region, the separation region, also, travels farther downstream, reducing the size of the wake and the magnitude of the pressure drag.

5.2.3. Skin Friction Coefficient ($C_{f,m}$). The distribution of average skin friction coefficient around wing-shaped tubes bundle is studied. Figures 19 and 20 show the effect of h_f on average $C_{f,m}$ at different Re_a for wing-shaped tubes bundle. $C_{f,m}$ decreases as Re_a increases. It can be observed that there is no significant difference in the values of $C_{f,m}$ for different arrangements at considered Re_a .

This phenomenon may be explained as follows. For the baseline case NOF, the air flow resistance from the inlet to outlet of the heat exchanger arises from the local resistance of the wing-shaped tubes, which plays dominant part of the total pressure drop. When the LFTHs are installed, the air flow resistance will arise from the tubes and the local resistance of the LFTH. LFTH brings about additional form drag and delays the separation of boundary layer from the wing-shaped tubes and decreases the wake region behind

the tube so that the form drag from the tubes decreases. Therefore, the LFTH with $h_f = 6$ mm offers lower form drag than that with $h_f = 12$ mm and that of NOF. Thus, the case of $h_f = 6$ mm increases the heat transfer and decreases $C_{f,m}$ compared with the base case of NOF.

5.2.4. Selection of Best Arrangement for Lowest Pumping Power (PP). One of the goals of this study is to predict optimal h_f that would minimize the frictional losses of the flow. A typical plot is provided to compromise between h_f and the pumping power (PP). A relationship (4) was obtained on multiplying the pressure drop and the volumetric flow rate as

$$PP = \Delta P_a \cdot FR_{a,i}, \quad (4)$$

where ΔP is pressure drop (Pa). $FR_{a,i}$ is air volume flow rate (m^3/s).

Figure 21 shows the variation of PP versus Re_a at different h_f . It is seen from the figure that PP increases with the increase of Re_a for arrangements with different h_f . Figure 22 shows the effect of h_f on PP at different Re_a . At certain Re_a , PP decreases with h_f from $2 \text{ mm} \leq h_f \leq 6 \text{ mm}$, while the

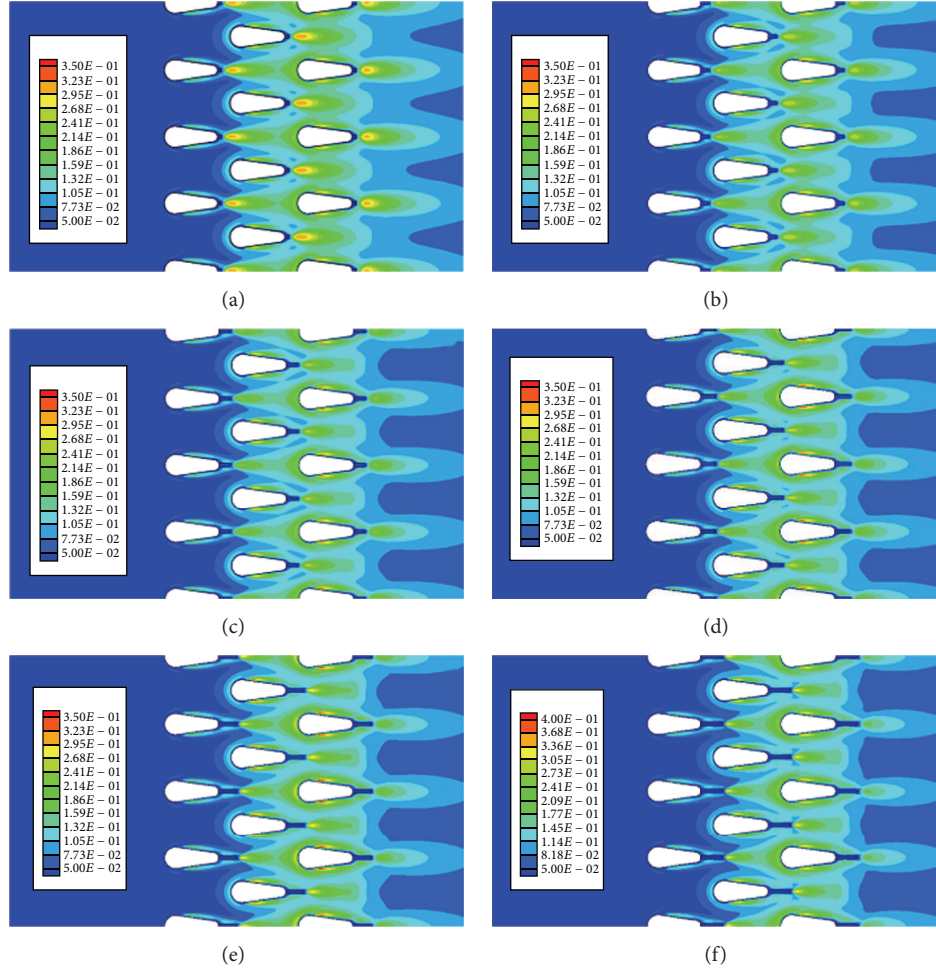


FIGURE 11: Turbulent kinetic energy contours (m^2/s^2) of the wing-shaped tubes for different fin heights (h_f) at $\text{Re} = 1800$: (a) $h_f = 2$ mm, (b) $h_f = 4$ mm, (c) $h_f = 6$ mm, (d) $h_f = 8$ mm, (e) $h_f = 10$ mm, and (f) $h_f = 12$ mm.

variation of PP is negligible for $6 \text{ mm} < h_f \leq 12 \text{ mm}$. The figure shows, also, that the lowest values of the pumping power are achieved for arrangements of $h_f = 6$ mm for the considered Re_a range.

This is due to the fact that the wing-shaped tubes bundle arrangement promoted turbulent mixing and lengthened the air flow path through the bundle. The size and the strength of the turbulence level as well as the reversed flow region are affected by h_f and Re_a variations.

5.3. Effect of δ at Constant ($h_f = 6$ mm) on ΔP_a and $C_{f,m}$. Figures 23 and 24 show the effect of δ on ΔP_a and $C_{f,m}$ for different Re_a at constant $h_f = 6$ mm. It is clear from Figure 23 that δ has negligible effect on $C_{f,m}$ and the highest values of $C_{f,m}$ are obtained for $\text{Re}_a = 1850$ while the lowest ones belong to $\text{Re}_a = 9700$. Figure 24 shows a variation in ΔP_a values for the considered δ range, where ΔP_a increases for $1.5 \text{ mm} \leq \delta \leq 2.5 \text{ mm}$ while ΔP_a decreases with $2.5 \text{ mm} < \delta \leq 3.5 \text{ mm}$ for the considered Re_a range except for $\text{Re}_a = 1850$ where there is no significant change of ΔP_a for $1.5 \text{ mm} \leq \delta \leq 3.5 \text{ mm}$.

6. Correlations of the Results

Correlations for P_{dc} and $C_{f,m}$ based on the numerical results obtained in terms of Re and h_f/D_{eq} are predicted by (5) and (6), using power regression, as follows:

$$P_{dc} = a + b(\text{Re}_a)^{-1} + c(\text{Re}_a)^{-2} + d\left(\frac{h_f}{D_{eq}}\right) + e\left(\frac{h_f}{D_{eq}}\right)^2, \quad (5)$$

$$C_{f,m} = a \cdot (\text{Re}_a)^b \cdot \left(\frac{h_f}{D_{eq}}\right)^c, \quad (6)$$

where D_{eq} is the equivalent circular diameter.

Table 1 shows all constants with maximum percentage difference (max. diff. %) between the calculated and obtained results for (5) and (6). The excellent R^2 values confirm the statistical goodness of the fit. The obtained correlations are applicable for $1.8 \times 10^3 \leq \text{Re}_a \leq 9.7 \times 10^3$.

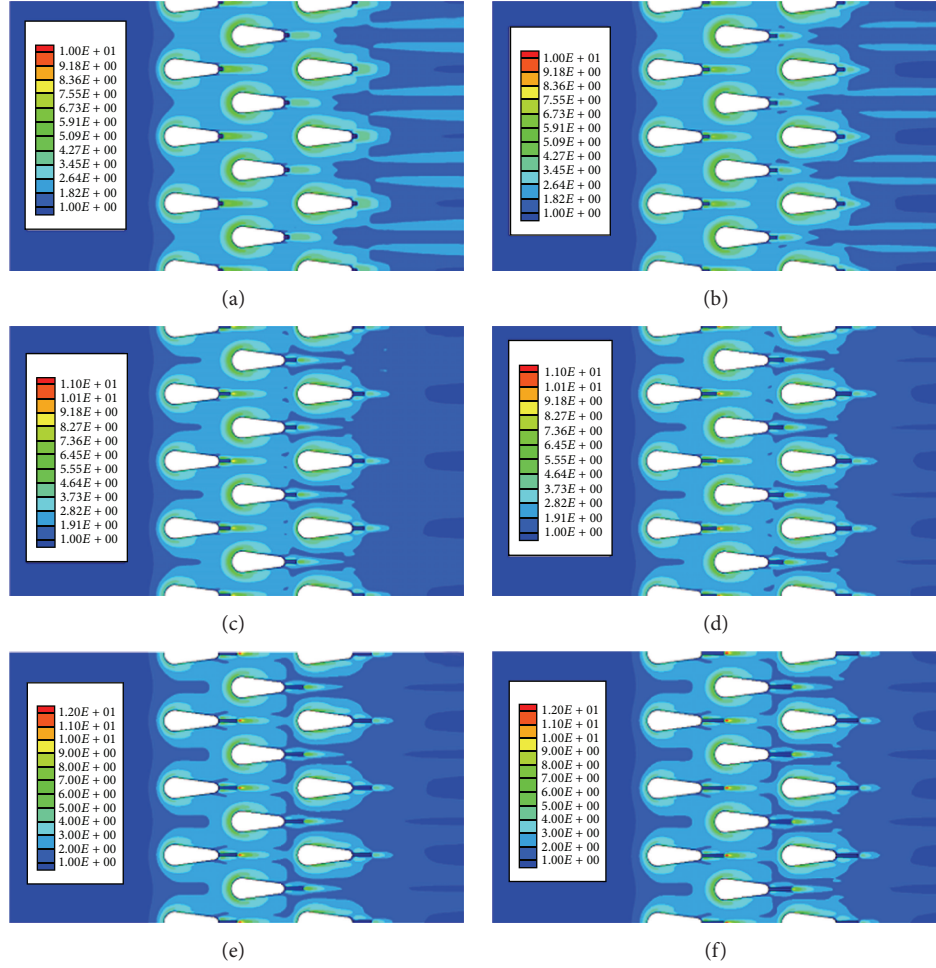


FIGURE 12: Turbulent kinetic energy contours (m^2/s^2) of the wing-shaped tubes for different fin heights (h_f) at $\text{Re} = 9700$: (a) $h_f = 2$ mm, (b) $h_f = 4$ mm, (c) $h_f = 6$ mm, (d) $h_f = 8$ mm, (e) $h_f = 10$ mm, and (f) $h_f = 12$ mm.

TABLE 1: Constants for (5) and (6).

| Equation number | a | b | c | d | e | R^2 | Max. diff. % |
|-----------------|-------|----------|----------------------|------|-------|-------|--------------|
| (5) | 1.47 | -4574.84 | 7416.5×10^3 | -1.1 | 1.823 | 0.9 | ± 9 |
| (6) | 1.042 | -0.405 | -5.203 | — | — | 0.99 | ± 4 |

7. Conclusions

Improvement of wing-shaped tubes bundle performance requires the elimination of fluid flow deficiency in certain regions over the tubes. This suggests the placement of extended surface in the deficient regions, where the separation of flow makes the heat transfer, mainly, by natural convection. A numerical study has been conducted to clarify fluid flow characteristics, pressure drop distributions, and $C_{f,m}$ over a wing-shaped tubes bundle in staggered arrangement with the placement of LF on downstream side of the tube. Re_a ranged from 1.8×10^3 to 9.7×10^3 . The tubes bundles are equipped with various fins having $2 \text{ mm} \leq h_f \leq 12 \text{ mm}$

and $1.5 \text{ mm} \leq \delta \leq 3.5 \text{ mm}$ at considered Re_a range. The flow pattern around the staggered wing-shaped tubes bundle is predicted using the commercial CFD FLUENT 6.3.26 software package. Correlations of pressure drop coefficient P_{dc} and skin friction coefficient ($C_{f,m}$) in terms of Re_a , design parameters, for the studied cases are presented. Comparisons between the experimental and numerical results of the present study and those, previously, obtained for similar available studies showed good agreements. Results indicate that the attaching of LF to the tubes surfaces downstream acts as a heat transfer cascade where heat transfers firstly by conduction through the fins and then followed by convection to the main flow downstream. The following conclusions are preferred:

- (i) ΔP_a increases with of Re_a for LF with different h_f . ΔP_a decreases with h_f for $2 \text{ mm} \leq h_f \leq 6 \text{ mm}$, while there is no significant change of ΔP_a for $6 \text{ mm} < h_f \leq 12 \text{ mm}$ except for slight increasing of ΔP_a at $6 \text{ mm} < h_f \leq 12 \text{ mm}$ for $\text{Re}_a = 9700$. Lowest values of ΔP_a occurred for arrangements of $h_f = 6 \text{ mm}$.

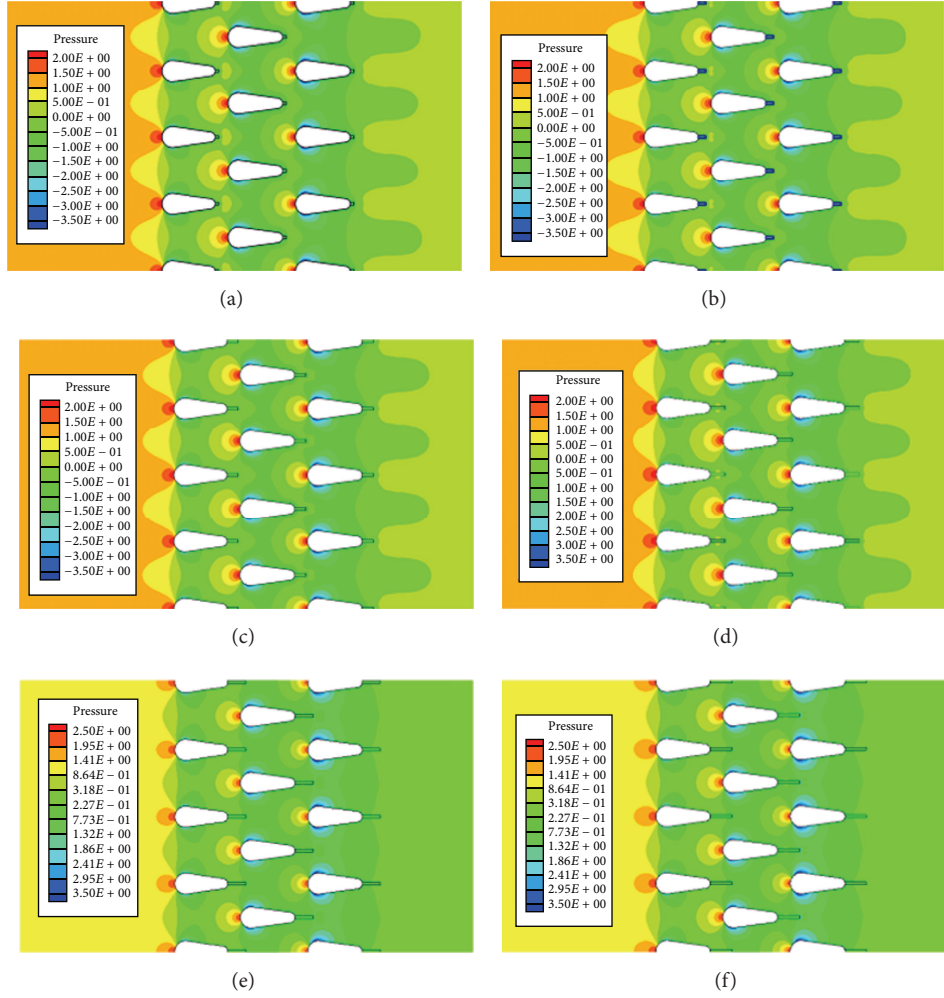


FIGURE 13: Static pressure contours (Pa) through the wing-shaped tubes bundle for different fin heights (h_f) at $Re = 1800$: (a) $h_f = 2$ mm, (b) $h_f = 4$ mm, (c) $h_f = 6$ mm, (d) $h_f = 8$ mm, (e) $h_f = 10$ mm, and (f) $h_f = 12$ mm.

- (ii) P_{dc} has the highest values for all studied h_f at $Re_a = 2000$, and P_{dc} decreases with the increase of Re_a in the range of $1800 \leq Re_a \leq 4200$ and then increases for $4200 \leq Re_a \leq 10000$ for all tested fins. Lowest values of P_{dc} occurred at $h_f = 6$ mm.
- (iii) P_{dc} decreases with h_f for $2 \text{ mm} \leq h_f \leq 6$ mm, while P_{dc} increases for $6 \text{ mm} < h_f \leq 12$ mm with considered Re_a . The values of P_{dc} for $h_f = 6$ mm are lower than those of NOF and $h_f = 2$ mm by about 73% and 32%, respectively, at $Re_a = 4000$.
- (iv) $C_{f,m}$ decreases as Re_a increases for all studied fins. The use of LF with $h_f = 6$ mm results in decreasing average $C_{f,m}$ compared with these of the case of NOF.
- (v) PP increases with the increase of Re_a for arrangements with different h_f . PP decreases with h_f from $2 \text{ mm} \leq h_f \leq 6$ mm, while the variation of PP is negligible for $6 \text{ mm} < h_f \leq 12$ mm. The lowest values of PP are achieved for arrangements of $h_f = 6$ mm for the considered Re_a range.
- (vi) δ has negligible effect on $C_{f,m}$ and the highest values of $C_{f,m}$ are obtained for $Re_a = 1850$ while the lowest ones belong to $Re_a = 9700$.
- (vii) ΔP_a increases for $1.5 \text{ mm} \leq \delta \leq 2.5$ mm while ΔP_a decreases with $2.5 \text{ mm} < \delta \leq 3.5$ mm for the considered Re_a range except for $Re_a = 1850$, where there is no significant change of ΔP_a for $1.5 \text{ mm} \leq \delta \leq 3.5$ mm.
- (viii) Correlations for P_{dc} and $C_{f,m}$ based on the numerical results are obtained in terms of Re_a and h_f/D_{eq} .

The Resultant Point of View. The above-mentioned discussion showed that the wing-shaped tubes bundle heat exchanger with $h_f = 6$ mm has the lowest values of ΔP_a , P_{dc} , C_f , and PP and hence the best performance comparing with the other bundles.

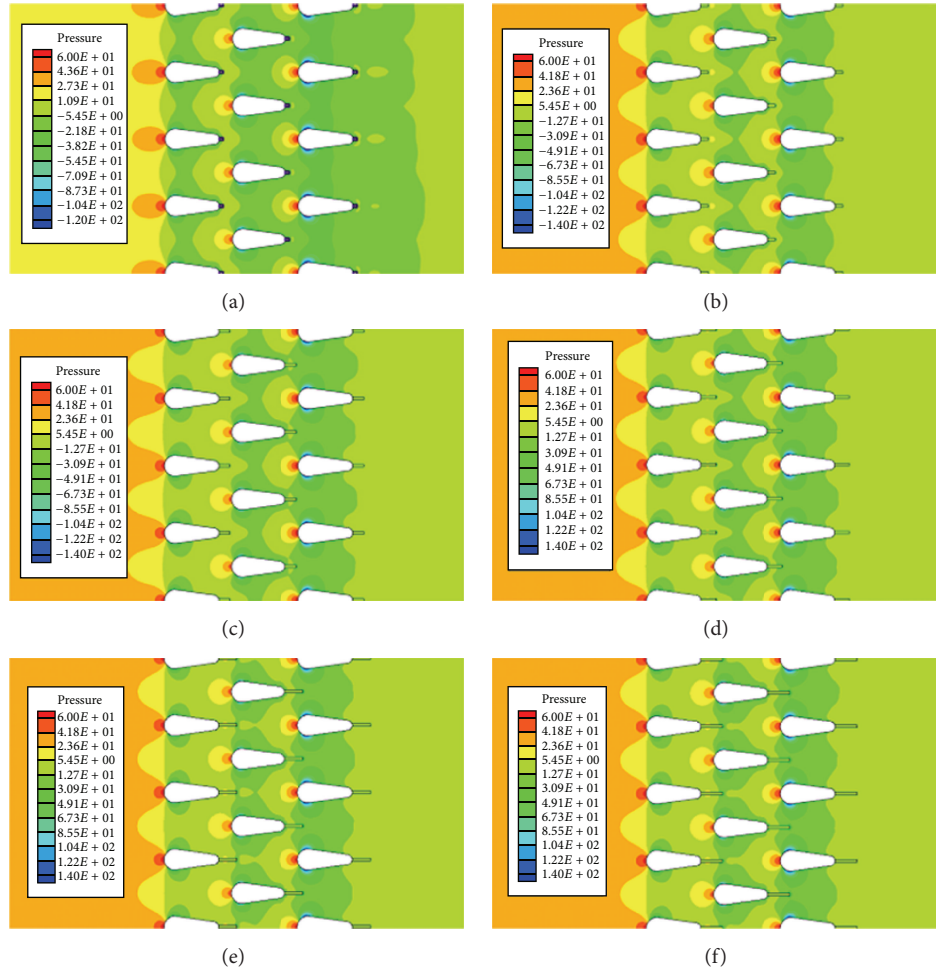


FIGURE 14: Static pressure contours (Pa) through the wing-shaped tubes bundle for different fin heights (h_f) at $Re = 9700$: (a) $h_f = 2$ mm, (b) $h_f = 4$ mm, (c) $h_f = 6$ mm, (d) $h_f = 8$ mm, (e) $h_f = 10$ mm, and (f) $h_f = 12$ mm.

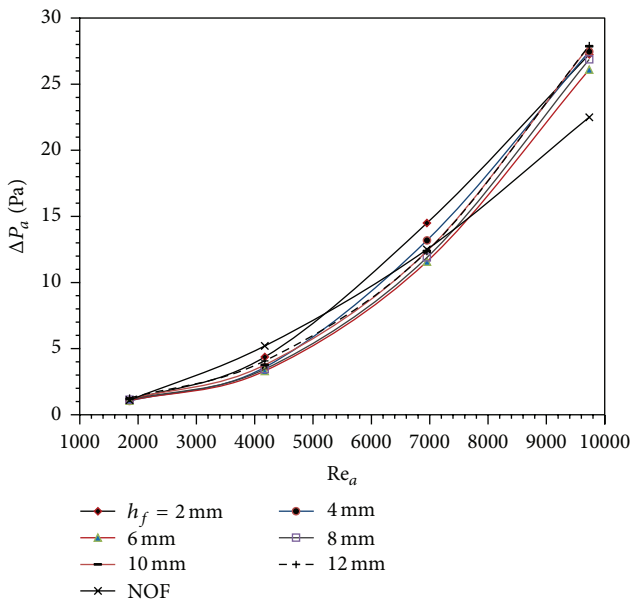


FIGURE 15: Variation of ΔP_a versus Re_a at different fin height.

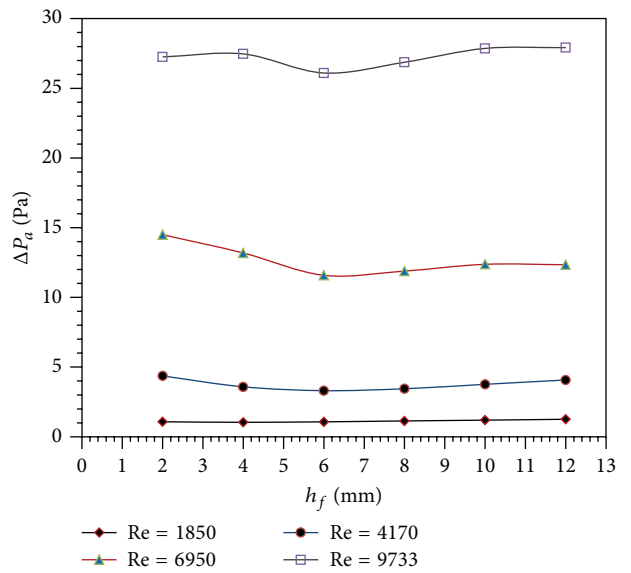


FIGURE 16: Variation of ΔP_a versus h_f at different Re_a .

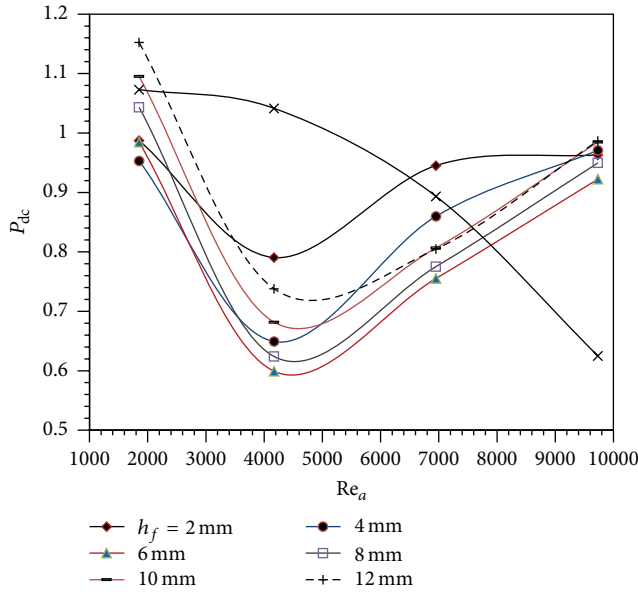


FIGURE 17: The effect of Re_a on P_{dc} for different h_f .

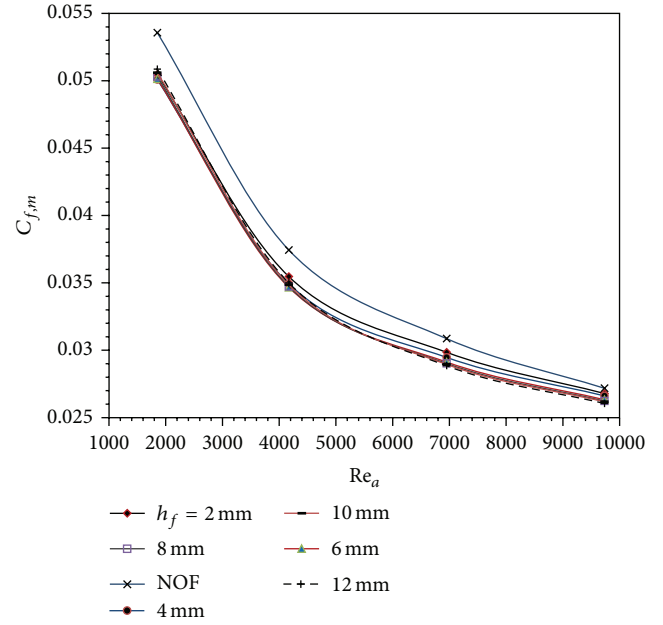


FIGURE 19: Variation of average skin friction coefficient ($C_{f,m}$) versus Re_a at different h_f .

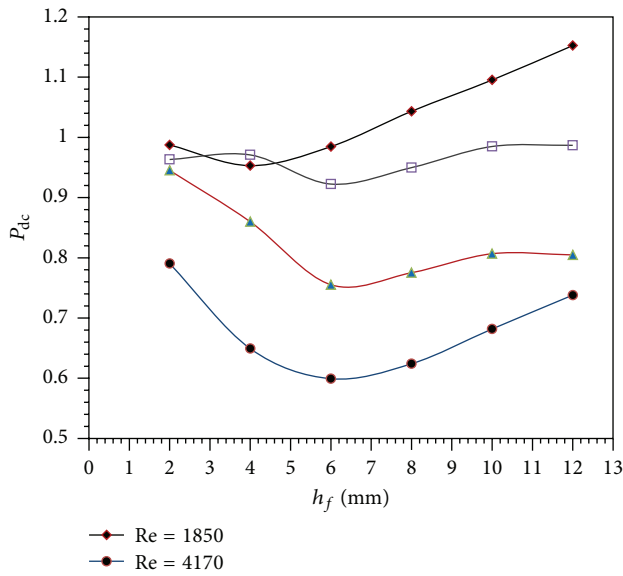


FIGURE 18: The effect of h_f on P_{dc} for different Re_a .

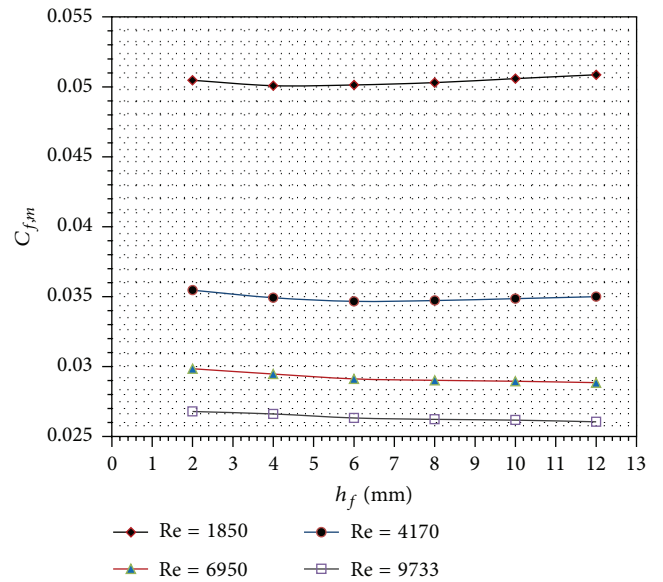


FIGURE 20: Effect of h_f on average skin friction coefficient ($C_{f,m}$) at different Re_a .

Symbols

Alphabet: Upper Case

PP: Pumping power, W

A_{so} : Total outer surface area of the tubes, m^2

D_{eq} : Equivalent circular diameter, m

F_p : Fin pitch, m (fin spacing + fin thickness)

S: Fin spacing, m

P_{dc} : Pressure drop coefficient, $(2 \cdot \Delta P_a) / (\rho_{af} \cdot V_a^2)$

R^2 : Coefficient of determination ranged from 0 to 1

Re: Reynolds number, $(\rho \cdot V \cdot D_{eq}) / \mu$

T: Temperature, K

V: Velocity, m/s

S_L : Longitudinal tube pitch, m

S_T : Transverse tube pitch, m

S_w : Slit width, m

L_l : Louver length, m

L_p : Louver pitch, m

B: Surface emissivity parameter, dimensionless.

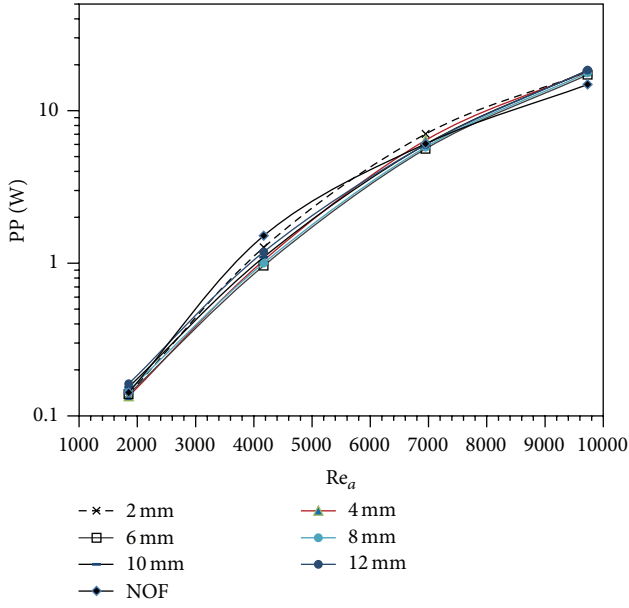


FIGURE 21: Effect of Re_a on pumping power (PP) for different h_f .

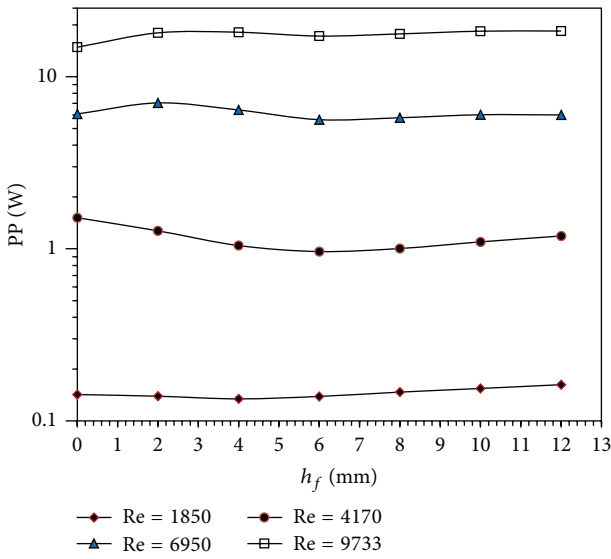


FIGURE 22: Effect of h_f on pumping power (PP) at different Re_a .

Alphabet: Lower Case

- c_p : Specific heat at constant pressure, J/kg·K
- h : Heat transfer coefficient, W/m²·K
- k : Thermal conductivity, W/m·K
- m : Mass flow rate, kg/s
- t : Tube thickness, m
- x : Axial coordinate
- y : The normal distance to the tube surface
- y^+ : Dimensionless normal distance to the tube surface
- h_f : Fin height, m.

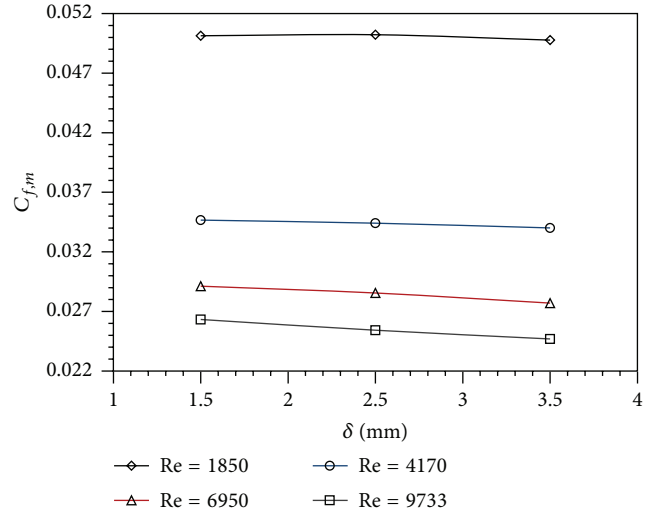


FIGURE 23: Effect of δ on $C_{f,m}$ for different Re_a at $h_f = 6$ mm.

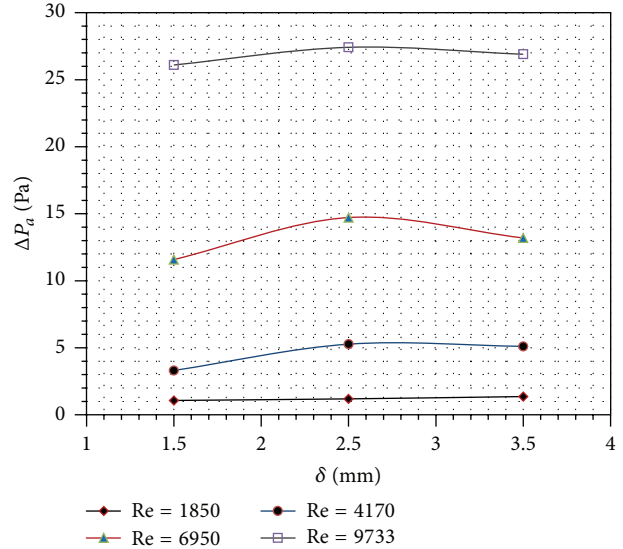


FIGURE 24: Effect of δ on ΔP_a for different Re_a at $h_f = 6$ mm.

Greek Symbols

- μ : Absolute viscosity, Pa·s
- θ : Louver angle, °
- ρ : Density, kg/m³
- ΔP_a : Pressure drop across the bundle, Pa
- Φ : Irreversibility ratio
- η_f : Fin efficiency
- δ : Fin thickness, m.

Subscripts

- a : Air
- c : Circular
- e : Exit
- f : Film or fin

i: Inlet or row number
o: Outer or outlet
h: Height
L: Longitudinal.

Abbreviations

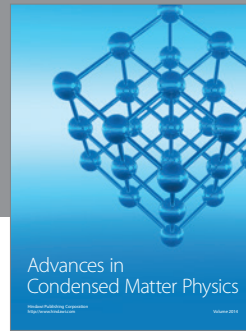
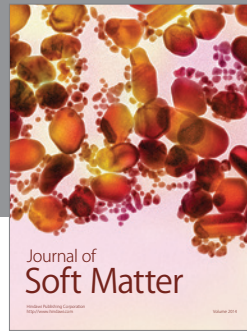
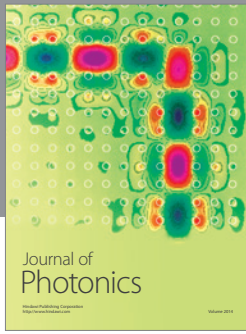
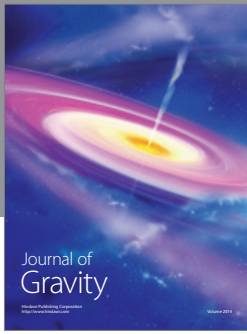
RNG: Reynolds normalized group
 LFTH: Longitudinal finned tubes heat exchanger
 NOF: Without fin
 DTM: Differential transformation method.

Conflict of Interests

The authors declare that there is no conflict of interests regarding the publication of this paper.

References

- [1] H.-T. Chen, J.-C. Chou, and H.-C. Wang, "Estimation of heat transfer coefficient on the vertical plate fin of finned-tube heat exchangers for various air speeds and fin spacings," *International Journal of Heat and Mass Transfer*, vol. 50, no. 1-2, pp. 45–57, 2007.
- [2] J.-Y. Jang, M.-C. Wu, and W.-J. Chang, "Numerical and experimental studies of three-dimensional plate-fin and tube heat exchangers," *International Journal of Heat and Mass Transfer*, vol. 39, no. 14, pp. 3057–3066, 1996.
- [3] C.-C. Wang, Y.-J. Chang, Y.-C. Hsieh, and Y.-T. Lin, "Sensible heat and friction characteristics of plate fin-and-tube heat exchangers having plane fins," *International Journal of Refrigeration*, vol. 19, no. 4, pp. 223–230, 1996.
- [4] A. F. Khudheyer and M. S. Mahmoud, "Numerical analysis of fin-tube plate heat exchanger by using CFD technique," *Journal of Engineering and Applied Sciences*, vol. 6, no. 7, pp. 1–12, 2011.
- [5] M. V. Ghorri and R. K. Kirar, "Numerical analysis of tube-fin heat exchanger using fluent," *International Journal on Theoretical and Applied Research in Mechanical Engineering*, vol. 1, no. 2, pp. 37–44, 2012.
- [6] W.-M. Yan and P.-J. Sheen, "Heat transfer and friction characteristics of fin-and-tube heat exchangers," *International Journal of Heat and Mass Transfer*, vol. 43, no. 9, pp. 1651–1659, 2000.
- [7] I. Wolf, B. Frankovic, I. Vilicic, R. Jurkowski, and A. Bailly, "A numerical and experimental analysis of heat transfer in a wavy fin and tube heat exchanger," in *Energy and the Environment*, pp. 91–101, 2006.
- [8] L. H. Tang, M. Zeng, and Q. W. Wang, "Experimental and numerical investigation on air-side performance of fin-and-tube heat exchangers with various fin patterns," *Experimental Thermal and Fluid Science*, vol. 33, no. 5, pp. 818–827, 2009.
- [9] J.-S. Leu, M.-S. Liu, J.-S. Liaw, and C.-C. Wang, "A numerical investigation of louvered fin-and-tube heat exchangers having circular and oval tube configurations," *International Journal of Heat and Mass Transfer*, vol. 44, no. 22, pp. 4235–4243, 2001.
- [10] C. T'Joene, H. Huisseune, H. Canire, H. J. Steeman, A. Willockx, and M. De Paepe, "Interaction between mean flow and thermohydraulic behaviour in inclined louvered fins," *International Journal of Heat and Mass Transfer*, vol. 54, no. 4, pp. 826–837, 2011.
- [11] W. Li and X. Wang, "Heat transfer and pressure drop correlations for compact heat exchangers with multi-region louver fins," *International Journal of Heat and Mass Transfer*, vol. 53, no. 15-16, pp. 2955–2962, 2010.
- [12] E. M. Sparrow and S. S. Kang, "Longitudinally-finned cross-flow tube banks and their heat transfer and pressure drop characteristics," *International Journal of Heat and Mass Transfer*, vol. 28, no. 2, pp. 339–350, 1985.
- [13] E. Ibrahim and M. Moawed, "Forced convection and entropy generation from elliptic tubes with longitudinal fins," *Energy Conversion and Management*, vol. 50, no. 8, pp. 1946–1954, 2009.
- [14] M. Torabi and Q. B. Zhang, "Analytical solution for evaluating the thermal performance and efficiency of convective-radiative straight fins with various profiles and considering all nonlinearities," *Energy Conversion and Management*, vol. 66, pp. 199–210, 2013.
- [15] Z. Hu and D.-W. Sun, "Predicting local surface heat transfer coefficients by different turbulent k- ϵ models to simulate heat and moisture transfer during air-blast chilling," *International Journal of Refrigeration*, vol. 24, no. 7, pp. 702–717, 2001.
- [16] V. Yakhot, S. A. Orszag, S. Thangam, T. B. Gatski, and C. G. Speziale, "Development of turbulence models for shear flows by a double expansion technique," *Physics of Fluids A*, vol. 4, no. 7, pp. 1510–1520, 1992.
- [17] *FLUENT 6.3.26 User's Guide*, FLUENT Inc, 2006.
- [18] E. S. Sayed Ahmed, E. Z. Ibrahim, O. M. Mesalhy, and M. A. Abdelatif, "Effect of attack and cone angles on air flow characteristics for staggered wing shaped tubes bundle," *Heat and Mass Transfer*, vol. 51, no. 7, pp. 1001–1016, 2015.
- [19] S. A. E. Sayed Ahmed, E. Z. Ibrahim, O. M. Mesalhy, and M. A. Abdelatif, "Heat transfer characteristics of staggered wing-shaped tubes bundle at different angles of attack," *Heat and Mass Transfer*, vol. 50, no. 8, pp. 1091–1102, 2014.



Hindawi

Submit your manuscripts at
<http://www.hindawi.com>

